Experimental research of circular incoherently synthetic aperture imaging ladar using chirped-laser and heterodyne detection

Yi Yan (严 毅), Jianfeng Sun (孙建锋)*, Xiaofeng Jin (金晓峰), Yu Zhou (周 煜), Yanan Zhi (职亚楠), and Liren Liu (刘立人)

Key Laboratory of Space Laser Communication and Testing Technology, Shanghai Institute of Optics and Fine Mechanics, Chinese Academy of Sciences, Shanghai 201800, China

**Corresponding author: sunjianfengs@163.com*

Received February 15, 2012; accepted March 28, 2012; posted online July 13, 2012

Synthetic aperture imaging ladar (SAIL) technique belongs fully coherent processing in both the time domain and space domain and has a rather high implement difficulty. To solve this problem, the concept of circular incoherently SAIL is introduced. A speckle version image of a two-dimensional (2D) letter 'E' target is reconstructed from E-field projection data detected by a circular incoherently SAIL system. The experimental system is constructed by three subsystems using chirped-pulse laser as the light source and heterodyne detection to get the range information of the target. The reconstruction of the image and the noise effect are also discussed in detail.

OCIS codes: 110.3010, 280.3640, 110.2970.
doi: 10.3788/COL201210.091101.

The technique of high resolution imaging from a long distance has been pursued by researchers for many years, and many different imaging methods have been developed, in which the most promising method is the synthetic aperture imaging ladar (SAIL) technique[1]. SAIL technique integrates reflective information of the target from different angles in coherent ways and can provide the centimeter-class resolution with an aperture size no larger than a few meters on an observation range of thousand kilometers or more. But the SAIL technique belongs fully coherent processing in both the time domain and space domain, and has a rather high implement difficulty. To solve this problem, the concept of circular incoherently SAIL technique is introduced in this letter.

The circular operating mode is one of the spotlight-modes in synthetic aperture radar (SAR), which is based on the relative rotation between the radar and target. It is first proposed by M. Soumekh[2,3]. After that, Tsz-King Chan *et al.* proposed a confocal algorithm for circular SAR[4−6]. Experiment of radar division of Georgia Tech Research Institute[7−9] and Technische Universitat Miinchen[10−13] has proved the feasibility of circular trajectory in signal collecting. The circular incoherently SAIL collects 360° data of projections around the target, and a two-dimensional (2D) image of the object is reconstructed by tomography algorithm from incoherent processing. Compared with other spotlight-modes, circular scanning trajectory breaks up the restriction on the extent of spatial spectrum, and as a result, high resolution image can be acquired from the circular incoherently SAIL.

In this letter, we propose a circular incoherently SAIL experimental system which can get the image of the whole target region covered by the laser beam. In the experiment, a 2D target of letter "E" is placed on a plane with a tilt angle to the horizontal plane and rotated about the axis perpendicular to the tilt plane. During the experiment, the target is illuminated by a linear FM laser, and the range-dependent return signal is collected by a heterodyne detective optical system. Filtered back-projection tomography algorithm is used to reconstruct the target, and a speckle version image result which has distinct feature description of the target is obtained.

For an incoherently SAIL, the range-resolved are first collected by the rotated side looking projections from the object illuminated with a laser beam and the image is reconstructed by virtue of tomography algorithms. But in radar detection, instead of transmission information, only reflection information can be gotten, so back-projection reflective tomography algorithm[14,15] is appropriate for the data processing in incoherently circular SAIL. Let $f(x, y)$ denote the image to be reconstructed in reflective tomography and $L_{r,\phi}$ denote the solid line $r = x\cos\phi + y\sin\phi$ (see Fig. 1)

$$p(r, \phi) = \int_{L_{r,\phi}} f(x, y)\mathrm{d}s, \tag{1}$$

where s represents the solid line along $L_{r,\phi}$, $p(r, \phi)$ is the projection of target $f(x, y)$ at angle ϕ, and r denotes the spatial variable along the integration path in the ϕ direction.

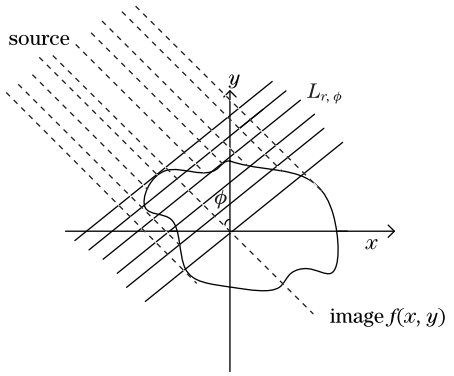

Fig. 1. Sketch of filtered back-projection algorithm.

Using back-projection algorithm, the estimated image $g(x, y)$ can be obtained as

$$g(x,y) = \sum_{i=1}^{m} p(x\cos\phi_i + y\sin\phi_i, \phi_i)\Delta\phi, \tag{2}$$

where ϕ_i is the angle of the ith projection, $\Delta\phi$ is the angular sampling interval, and m is the total number of projections. Filtered back-projection is used to modify projections and reduce star-like artifacts. The reconstructed image $g_{\mathrm{FB}}(x, y)$ can be given as

$$g_{\mathrm{FB}}(x,y) = \sum_{i=1}^{m} \mathcal{F}^{-1}\{|v|\mathcal{F}[p(x\cos\phi_i + y\sin\phi_i, \phi)]\}\Delta\phi, \tag{3}$$

where $\mathcal{F}$ and $\mathcal{F}^{-1}$ denote the one-dimensional Fourier transform and the inverse Fourier transform operators, respectively, and ν represents frequency variable.

Determine the sampling interval is an essential procedure in reflective tomography[16]. Supposing $x_{\max}$ is space-limited extent of the target $f(x, y)$, $u_{\max}$ as the cutoff frequency of $F(u_1, u_2)$, the spacing between angles over the projection data collected can be calculated. Let $\Delta\phi$ be the angular spacing between the tomographic views, it is approximately given by

$$\Delta\phi \leqslant \frac{1}{x_{\max}u_{\max}}. \tag{4}$$

The total number N_ϕ of projections needed to obtain an accurate reconstruction of image $g(x, y)$ is determined by the total angular extent

$$N_\phi \geqslant \frac{\pi}{\Delta\phi} = \pi x_{\max}u_{\max}. \tag{5}$$

The sampling number N_{p} needed in the projection data for each angle can be determined by

$$N_{\mathrm{p}} \geqslant \frac{x_{\max}}{1/(2u_{\max})} = 2x_{\max}u_{\max}. \tag{6}$$

The system configuration[17,18] for our experiment is shown in Fig. 2. The system consists of three subsystems: the light source system, the T/R antenna system, and the signal acquisition system. A tunable external-cavity semiconductor laser is used as the signal source. A single-mode and polarizing-maintained fiber amplifier amplifies the power of the source signal. The signal coming from the fiber amplifier is then split into two separate paths. The main power is led to the T/R antenna system, where one serves as signal and the other as local oscillator signal.

The heterodyne detective demonstrator is configured as a deramp-on-receive system, in which a time-delayed version of the signal is mixed with echoes received from target. The deramp-on-receive method can reduce the bandwidth needed for the receiving system. The signal and local oscillator signal are exported by collimators to free space with diameters of 2.1 mm. The half-wave plates behind the collimators are used to optimize the transmission efficiency in polarization beam splitter (PBS) 1. Then, the diameters of the signals are expanded to 20 mm using a secondary telescope and then to 300 mm using the main telescope. PBS2 is used as a duplexer for transmitting the signal and reflecting the echoes from the target. The half-wave plates behind PBS2 are used to change the polarization state of the echoes as the polarization state can often be rotated after being reflected by the target. The echoes and local oscillator signal are combined in PBS3 and spatially filtered using a reception diaphragm. A 200×200 (mm) rectangular diaphragm placed on the exit pupil of the main telescope is used to obtain a rectangular spot on the target plane. The distance from the center of the target to the exit pupil is 14 m. The balanced optical signal from the combined local oscillator signal and echoes are then focused on a detector in a balanced receiver. The target is a 11×11 (mm) letter "E" cut from a retroreflective material (Series 983D, 3M Super High Intensity Grade micro prismatic sheeting), which is mounted at a tilt angle of 45° from the horizontal plane. During the experiment, the target is rotated about the axis perpendicular to the tilted plane. The specific details of the target are shown in Fig. 2.

Considering one angle of the experiment process, we suppose that, in the time domain, the linear FM chirp transmit signal is described as[19]

$$s(t) = \exp[\mathrm{j}(\omega_0 t + \alpha t^2)], \tag{7}$$

where ω_0 is the carrier wave frequency and α is the chirp rate of the signal.

By mixing the in-phase and quadrature local oscillator signals

$$\begin{aligned} c_{\mathrm{I}}(t) &= \cos[\omega_0(t-\tau_0) + \alpha(t-\tau_0)^2], \\ c_{\mathrm{Q}}(t) &= -\sin[\omega_0(t-\tau_0) + \alpha(t-\tau_0)^2], \end{aligned} \tag{8}$$

we can obtain the combined mixer output as the scatter signal received by the radar, which can be represented as

$$\begin{aligned} r(t) = A\mathrm{Re}\Bigg\{\int_{-u_1}^{u_1} f(u)\exp\{\mathrm{j}\{\omega_0[t-\tau_0-\tau(u)] \\ + \alpha[t-\tau_0-\tau(u)]^2\}\}\mathrm{d}u\Bigg\}, \end{aligned} \tag{9}$$

where A is a scale factor that accounts for propagation attenuation and other effects, $f(u)$ is the reflectivity density function, τ_0 is the time delay of the target center, u is the slant range distance from the target center x_0, and u varies from $-u_1$ to u_1, as shown in Fig. 3.

If we ignore the quadratic phase term that has little influence in a range-resolved situation, we can write the mixer output signal as

$$\overline{r}(t) = \frac{A}{2}\int_{-u_1}^{u_1} f(u)\exp\left\{\mathrm{j}\left\{-\frac{2u}{c}[\omega_0 + 2\alpha(t-\tau_0)]\right\}\right\}\mathrm{d}u. \tag{10}$$

Notice that the integrand of Eq. (10) involves the general form of the Fourier transform kernel, $\exp(-\mathrm{j}uU)$, where

$$U = \frac{2}{c}[\omega_0 + 2\alpha(t-\tau_0)]. \tag{11}$$

The equation indicates that the processed return chirp signal is the precise Fourier transform of the reflective function of the target. Consequently, the E-field frequency information of the target reflective function can be obtained from the processed signal at the fixed angle.

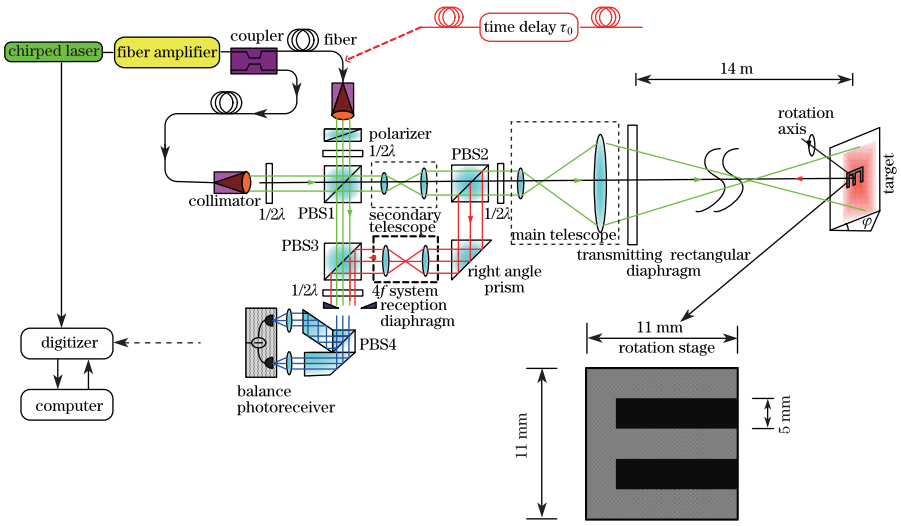

Fig. 2. Schematic diagram of experimental setup.

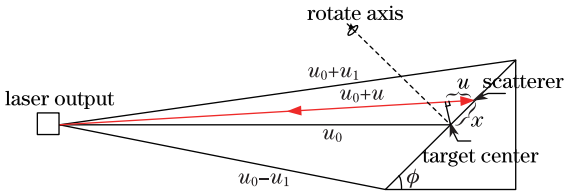

Fig. 3. Collection geometry.

In the experiment, the transmitting power of the tunable laser is approximately 1 mW at 1.5 μm, and the wavelength chirps from 1 549 to 1 553 nm with a chirp rate of 100 nm/s. The maximum difference frequency

$$\Delta f_n = \alpha_{\rm f}\frac{2x_{\max}}{c}\cos\phi = 2\frac{\alpha_\lambda}{\lambda^2}x_{\max}\cos 45^\circ$$
$$= \frac{10^5}{1.2}\times 11\times 10^{-3}\times 0.707 = 648\ \text{Hz}, \quad (12)$$

where $\alpha_{\rm f}$ is the frequency chirp rate, α_λ is the wavelength chirp rate, and ϕ represents the tilt angle of the target to the horizontal plane.

The relative rotation between target and reflective tomography ladar can be seen in Fig. 4, suppose that the basic reference plane $x-y$ is perpendicular to the incident light and that the target plane coordinate is represent by $x'-y'$. Then the distance from the exit pupil to the basic reference plane can be written as a constant Z. The angle between the base and target planes is $\frac{\pi}{2}-\varphi$, and an incident point (x, y) vertical to the basic reference plane has its coordinates on the target plane as

$$\begin{cases} x' = x \\ y' = y\cos\left(\dfrac{\pi}{2}-\varphi\right) = y\sin\varphi \end{cases}. \quad (13)$$

We denote the rotating angle as $\Delta\theta$, the contour equation of the target distance on the basic reference plane is

$$y = x\tan\Delta\theta + z_k, \quad (14)$$

where z_k represents the discrete range value. Taking Eq. (13) into consideration, we have

$$y' = \frac{x'\tan\Delta\theta + z_k}{\sin\varphi}. \quad (15)$$

From Eq. (15), we can obtain the contour equation of the range on the target plane with a rotation angle of $\Delta\theta$. The signals reflected by the same contour will superimpose with each other, and the signals reflected by different contours will separate from each other. Thus, the range projection can be calculated at the fixed angle $\Delta\theta$, with the range information represented by the heterodyne frequency[20].

In the experiment, the range extent of the target is

$$x_{\max} = 11\ \text{mm}. \quad (16)$$

According to Eq. (11), the slant range resolution determined by the signal acquisition system is

$$\rho_u = \frac{c}{2B_{\rm c}} = \frac{c}{2\alpha t} = 0.3\ \text{mm}, \quad (17)$$

where $B_{\rm c}$ is the bandwidth of the signal.

The actual range resolution of the target plane is

$$\rho_x = \rho_u/\cos\phi = 0.42\ \text{mm}. \quad (18)$$

From Eq. (4), the angular spacing $\Delta\phi$ can be given by

$$\Delta\phi \leqslant \frac{1}{x_{\max}u_{\max}} = \frac{\rho_x}{x_{\max}} = 2.18^\circ. \quad (19)$$

The total number of views needed is

$$N \geqslant \frac{2\pi}{\Delta\phi} = 165.13. \quad (20)$$

However, in image reconstruction, as the tomographic algorithm will improve the resolution of the reconstructed image, the angular spacing in our experiment should be smaller than the theoretical value. For convenience and accuracy, the sampling angular spacing is set as 1°.

During the experiment, the target rotates about the axis perpendicular to the bearing plane at 1° intervals. The reflected signal is collected while the target stays static at different angles, as shown in Fig. 5(a). Figure 5(b) shows the range contour of the target distance, and

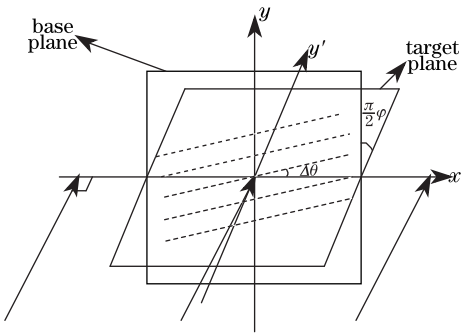

Fig. 4. Coordinate system for the rotation of target.

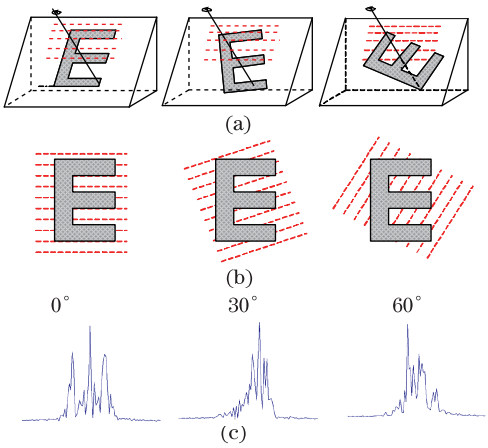

Fig. 5. Multiple angle reflective projections of the target: (a) static target of different angles, (b) range contour of the corresponding angles, and (c) received range projection of the corresponding angles.

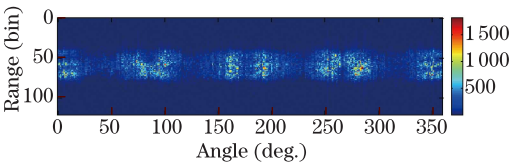

Fig. 6. Integrated image of 360° projections.

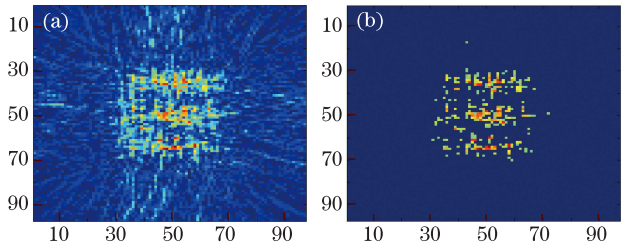

Fig. 7. Projection data and reconstructed image from the experiment: images (a) before and (b) after the filtering process.

the corresponding received range projection is shown in Fig. 5(c). Figure 6 shows the integrated image of 360° projections, in which x represents the angle and y represents the range of the signal. The range unit used is 1 bin = 0.42 mm, which corresponds to the range resolution of the system.

Reconstructed results from the experimental data are shown in Fig. 7. Compared with the conventional image obtained via reflective tomography, the reconstructed image has an apparent whole region of E. This reconstructed image can be interpreted as a speckle version image of the real 2D target because of the detective approach we adopted in the experiment. Although there were artifacts in the image reconstruction, the shape of the letter "E" was clearly recognized, and the size of the image reconstruction results matched well with the target. As is apparent, fair detail can be obtained using the reflective tomography algorithm.

In general, three kinds of noises should be considered in ladar systems: detection noises other than photon noise, photon noise, and laser-speckle noise. Detection noises other than photon noise can be neglected because a heterodyne detection system is used. Therefore, most of the noise in the reconstructed image of the E-field detective is laser speckle, which is very common in the heterodyne detection system and difficult to eliminate. However, as shown in Ref. [21], the offset portion of the Fourier transform contains image-domain information of reasonable quality because of speckle noise. As shown in Fig. 8, the resulting image has noticeable speckling, but this speckle precisely makes the recovery of low-frequency image information possible. The speckle size is orders of magnitude smaller than the overall image size and many of the image features. Thus, the eye can clearly see the image features to a certain extent[22].

Another important factor that affects image quality is the inaccurate time delay of the oscillator signal. In practice, determining the platform positions for the required tolerances over the entire flight time can be a difficult task. Even in the laboratory experiment, the platform vibration or propagating disturbance can cause interference and the time delay generated by the fiber loop may not be stable all the time. These time demodulation errors can be denoted as ε. Thus, instead of mixing the return signal with the expressions given by Eq. (8), the return signal is mixed with

$$\begin{cases} c_{\mathrm{I}}(t) = \cos[\omega_0(t-\tau_0+\varepsilon)+\alpha(t-\tau_0+\varepsilon)^2] \\ c_{\mathrm{Q}}(t) = -\sin[\omega_0(t-\tau_0+\varepsilon)+\alpha(t-\tau_0+\varepsilon)^2] \end{cases}. \quad (21)$$

The output of the demodulator then becomes

$$\begin{aligned} F_\varepsilon(U) &= \mathrm{e}^{-\mathrm{j}\varepsilon^2\alpha}\mathrm{e}^{\mathrm{j}\frac{\varepsilon c}{2}U}\int_{-u_1}^{u_1} f(u)\mathrm{e}^{-\mathrm{j}uU}\mathrm{d}u \\ &= \mathrm{e}^{-\mathrm{j}\varepsilon^2\alpha}\mathrm{e}^{\mathrm{j}\frac{\varepsilon c}{2}U}F(U). \end{aligned} \quad (22)$$

As discussed earlier, the output of the mix demodulator can be seen as the Fourier transform of the reflective function of the target so that the time demodulation errors will result in

$$\begin{aligned} f_\varepsilon(u) &= F^{-1}[F_\varepsilon(U)] = F^{-1}[\mathrm{e}^{-\mathrm{j}\varepsilon^2\alpha}\mathrm{e}^{\mathrm{j}\frac{\varepsilon c}{2}U}F(U)] \\ &= f\left(u+\frac{\varepsilon c}{2}-\varepsilon^2\alpha\right). \end{aligned} \quad (23)$$

From the equation, we can obtain a range shift in the reconstructed reflective function from

$$\delta u = \frac{\varepsilon c}{2}-\varepsilon^2\alpha. \quad (24)$$

If the slant range shifts of different angles are different because of the time demodulation errors, the reconstructed 2D image becomes corrupt and degrades because the target center of each projection is different when the reflective tomography algorithm is applied. To reduce the influence of the time demodulation error, we have to apply other measures, such as using inertial measurement units, installing a laser vibrametry system onboard, or applying feature tracking method and phase retrieval algorithm[23,24], to align projection data for image reconstruction in laboratory experiments.

Finally, the linearity of the FM chirped laser should also be considered. The chirped laser used is a wavelength chirp output instead of the desired frequency chirp output. The output of a wavelength modulation laser can be described as

$$\lambda = \lambda_0 + \dot{\lambda}\, t, \tag{25}$$

where λ_0 is the center-wavelength and $\dot{\lambda}$ is the wavelength chirp rate. Then, frequency can be written as

$$f = \frac{c}{\lambda} = \frac{c}{\lambda_0 + \dot{\lambda}\, t} = c\left(\frac{1}{\lambda_0} - \frac{\dot{\lambda}}{\lambda_0^2}t + \frac{\dot{\lambda}^2}{\lambda_0^3}t - \cdots\right). \tag{26}$$

Assuming that $f_0 = \frac{c}{\lambda_0}$ is the center frequency of the laser output, $\dot{f} = \frac{c}{\lambda_0}(\frac{\dot{\lambda}}{\lambda_0})t$ will be the linearity frequency modulation term. However, we also find $\ddot{f} = \frac{c}{\lambda_0}(\frac{\dot{\lambda}}{\lambda_0})^2 t$ and other terms such as the residual high-order FM terms in the equation. These residual terms will cause the nonlinearity of signal FM and result in phase errors in heterodyne detection, eventually leading to the blurring of the target and further reduction of the imaging resolution of the range direction. Certain matched filtering algorithms can handle the problems presented in this letter, and details can be found in Ref. [25].

In conclusion, without involving signal phrase processing and spatial phrase processing in incoherent aperture synthesis, the configuration and operations of circular incoherently SAIL technique can be simplified. At the same time, circular scanning trajectory breaks up the restriction on the extent of spatial spectrum with straight line observing path and realizes the objective of further improving the resolution. In our experiment, the range resolution is highly enhanced by the use of linear FM chirp impulse signal and heterodyne detection, thus the system is suitable for application under strong interference circumstances. Circular incoherently SAIL expands the application scope of the SAIL, and has a high practical significance. Future research includes alleviating the speckle noises to obtain better reconstructed images, reducing the phase error's influence by post-processing algorithm, and getting more experimental results under different conditions.

This work was supported by the Key Laboratory of Space Laser Communication and Testing Technology of the Chinese Academy of Sciences and the National Nature Science Foundation of China (No. 61108069).

References

1. L. Liu, Proc. SPIE **7818,** 78180U (2010).
2. M. Soumekh, IEEE Trans. Image Processing **5,** 1252 (1996).
3. M. Soumekh, *Synthetic Aperture Radar Signal Processing with MATLAB Algorithm* (John Wiley & Sons, New York, 1999).
4. Tsz-King Chan and Yasuo Kuga, in *Proceedings of IEEE International Conference on Geoscience and Remote Sensing* 1138 (1997).
5. Akira Ishimaru, Tsz-King Chan, and Yasuo Kuga, IEEE Trans. Geoscience and Remote Sensing **36,** 1524 (1998).
6. Tsz-King Chan, Yasuo Kuga, and Akira Ishimaru, IEEE Trans. Geoscience and Remote Sensing, **37,** 2192 (1999).
7. M. L. Bryant, L. L. Gostin, and M. Soumekh, in *Proceedings of IEEE International Conference on Geoscience and Remote Sensing* 628 (2001).
8. M. L. Bryant, L. L. Gostin, and M. Soumekh, IEEE Trans. Aerospace and Electronic Systems **39,** 211 (2003).
9. K. Ranney and M. Soumekh, in *Proceedings of IEEE International Conference on Radar* 195 (2005).
10. J. Detlefsen, A. Dallinger, and S. Schelkshorn, in *Proceedings of 1st European Radar Conference* 279 (2004).
11. A. Dallinger, S. Schelkshorn, and J. Detlefsen, in *Proceedings of Conference Digest IRMMW 2004/THz* 521 (2004).
12. A. Dallinger, S. Schelkshorn, and J. Detlefsen, in *Proceedings of German Microwave Conference* 244 (2005).
13. J. Detlefsen, A. Dallinger, and S. Schelkshorn, in *Proceedings of IEEE 9th International Symposium on Spread Spectrum Techniques and Applications* 46 (2006).
14. J. K. Parker, E. B. Cralg, and D. I. Klick, Appl. Opt. **27,** 2642 (1988).
15. C. L. Matson, Opt. Commun. **137,** 343 (1997).
16. C. L. Matson and D. E. Mosley, Appl. Opt. **40,** 2290 (2001).
17. Y. Zhou, A. Yan, and L. Liu, Proc. SPIE **7468,** 74680S (2009).
18. J. Sun, X. Jin, and Y. Zhou, Proc. SPIE **7780,** 778017 (2010).
19. C. V. Jakowatz Jr. and D. E. Wahl, *Spotlight-Mode Synthetic Aperture Radar: A Signal Processing Approach* (Kluwer Academic Publishers, Massachusetts, 1996).
20. C. L. Matson, Opt. Commun. **186,** 69 (2000).
21. D. C. Munson Jr. and J. L. C. Sanz, IEEE **72,** 661 (1984).
22. B. G. Zogar, Chin. Opt. Lett. **9,** 071203 (2011).
23. X. Jin, J. Sun, Y. Yan, Y. Zhou, and L. Liu, Opt. Commun. **283,** 3475 (2010).
24. X. Jin, J. Sun, Y. Yan, Y. Zhou, and L. Liu, Chin. Opt. Lett. **9,** 12801 (2011).
25. N. Xu, L. Liu, and W. Lu, Optik **122,** 211 (2011).